ACCSCIENCE PUBLISHING

Materials Science in Additive Manufacturing

ORIGINAL RESEARCH ARTICLE

Phase transformations in additively manufactured high carbon-bearing steel

Thinh Huynh, Kevin Graydon, Nicolas Ayers, and Yongho Sohn*

Department of Materials Science and Engineering, University of Central Florida, Orlando, Florida, United States of America

Abstract

For high-carbon steels that are particularly sensitive to thermally induced phase transformations, the rapid solidification rates inherent to laser powder bed fusion (LPBF) offer a promising pathway to develop unconventional microstructures directly in the as-printed state. This study demonstrates the formation of a supersaturated austenitic matrix – engineered through carbon meta-stabilization and rapid solidification for subsequent heat treatments to develop complex, hierarchical microstructural constituents. A predominantly austenitic high-carbon steel, decorated with cellular segregation networks, was successfully fabricated using LPBF. Post-processing through cryogenic quenching and high-temperature solutionizing treatment, followed by low-temperature tempering, yielded a wide range of microstructures and hardness values. The cryogenically quenched sample exhibited a mixed microstructure of martensite, retained austenite, and cellularly segregated regions, achieving a hardness of 737 ± 31 HV. In contrast, the combination of solutionizing, cryogenic quenching, and tempering produced a multiphase matrix consisting of martensite, bainite, and austenite, with a hardness of 700 ± 20 HV. The insights gained into phase transformations and microstructural evolution during LPBF, along with secondary hardening via heat treatment, provide a foundation for developing tailored post-processing strategies for a broad class of hardenable steels produced by additive manufacturing.

Keywords: High-carbon steel; Laser powder bed fusion; Additive manufacturing; Austenite; Martensite; Bainite

***Corresponding author:**
Yongho Sohn
(yongho.sohn@ucf.edu)

Citation: Huynh T, Graydon K, Ayers N, Sohn Y. Phase transformations in additively manufactured high carbon-bearing steel. *Mater Sci Add Manuf*. 2024;4(2):025100011. doi: 10.36922/MSAM025100011

Received: March 5, 2025

1st revised: April 10, 2025

2nd revised: April 17, 2025

Accepted: April 18, 2025

Published online: May 15, 2025

1. Introduction

Laser powder bed fusion (LPBF) additive manufacturing (AM) can produce engineering components with enhanced performance-to-weight ratio, refine the microstructure through rapid solidification, and enable innovative design. However, not all commercially available alloys are considered compatible with LPBF. Developmental efforts for metallic alloys used in LPBF often face technical challenges in undesired flaw formation. Even some alloys deemed weldable in the traditional sense have exhibited cracking under rapid solidification and often require chemistry modification for crack mitigation.[1,2] Parts built by AM processes like LPBF experience a very specific thermal history.[3] Particularly for phase transformation-sensitive steels, rapid quenching from the liquid state could produce varying amounts of austenite and martensite across the

sample height.[4] Subsequent remelting and heating inherent to the layer-by-layer process also induce an intrinsic heat treatment that can alter the printed microstructure.[5] Therefore, the development of new alloys, specifically for the LPBF and other AM technologies, must consider the unique thermo-kinetic environment.

The literature concerning high carbon steels has been mainly limited to H13 steels,[6-9] with some reports of other carbon-bearing tool steels;[10-15] however, their microstructural development can be used as a basis for understanding the laser-material interaction in tool steels during LPBF. The cellular dendritic microstructure,[6] containing as much as 15 wt.% austenite, was observed in as-print H13, and as high as 3 wt.% in the tempered state.[16] Low fractions of M_3C carbides can also be found in the as-print condition,[16] while higher tempering temperatures precipitate the $M_{23}C_6$ carbides,[17] which can improve wear resistance. Holzweissig *et al.*[18] proposed that retained austenite in LPBF-processed H13 at a substrate preheat of 100°C can form through a mechanism analogous to the quenching and partitioning process. The remelting of previously transformed martensite, combined with continuous heat input, prevents the part from reaching the martensite finish temperature. With sufficient thermal energy – supported by modest substrate preheating – carbon can diffuse from the "quenched" martensite into untransformed austenite, promoting its stabilization and retention at ambient conditions. Other high-carbon-bearing steels, such as M2 high-speed steel, require high substrate temperature to produce dense and crack-free parts.[11,19] At a substrate pre-heat temperature of 500°C, H11 steel has been observed to transform to an upper bainite rather than the desired martensite.[12] While the use of high substrate preheating temperatures could be viable in mitigating detrimental cold cracking,[20] phase transformation at temperatures imposed by the high substrate temperature during LPBF could occur, which may require additional post-processing steps, such as austenitizing and tempering, to obtain the desired microstructure.

High-strength steels and other carbon-bearing steels can possess martensitic microstructures by taking advantage of the rapid solidification inherent in the LPBF process. However, good printability (i.e., no cold cracking) has been limited to low-alloy steels with low to medium levels of carbon concentrations.[5,21-23] Excellent printability for austenitic steels relies on a higher Ni equivalent than Cr equivalent in this type of steel, stabilizing the austenitic phase,[24] and is therefore inhibited from the martensitic transformation for strengthening. High austenite stabilization provided by high carbon concentrations in rapidly solidified steels produced by LPBF could give rise to an austenitic microstructure in the as-print condition. Hence, ultra-high-carbon steels may be printable without the need for elevated substrate preheating temperatures. This study demonstrates that carbon-induced stabilization of austenite, combined with the rapid solidification characteristics of LPBF, can yield a nearly fully austenitic microstructure in the as-printed condition – achieved without high substrate preheating. This approach offers a pathway to improve the printability of high-performance, ultra-high-carbon steels tailored for AM. The resulting austenitic matrix, with its enhanced ductility and resistance to cracking during LPBF, serves as an ideal precursor for subsequent heat treatments aimed at developing complex, hierarchical microstructures.

The primary objective of this work is to harness the synergistic effects of elevated carbon content and rapid solidification inherent to LPBF to produce a predominantly austenitic as-built microstructure, which can then be selectively transformed through post-processing. This study explores the subsequent phase transformations of the as-printed steel under cryogenic quenching and thermal treatment. We demonstrate that controlled heat treatments can convert the austenitic matrix into a tailored mixture of martensite, bainite, and retained austenite, yielding a microstructure with excellent hardness. These findings highlight the potential of LPBF for processing high-carbon steels and underscore the need for further exploration of this alloy class, which offers a promising combination of microstructural versatility and mechanical performance.

2. Materials and methods

2.1. Material selection

Figure 1A presents the time-temperature-transformation (TTT) diagrams, calculated using JMatPro™ (version 7.0), for an ultra-high-strength steel composition previously investigated for LPBF processing.[23,25,26] The diagrams consider varying carbon concentrations while assuming a prior austenite grain size of 50 μm.[25] Figure 1B displays the equilibrium phase fractions as a function of temperature, calculated using JMatPro™ (version 7.0) based on the nominal composition examined in this study. Increasing the carbon concentration effectively suppresses both the martensite start (M_s) temperature and the bainitic transformation curve, shifting them to lower temperatures. This behavior is consistent with the well-established role of carbon in stabilizing the austenite phase and hindering the diffusion-controlled transformation kinetics of ferrite and bainite. These effects are particularly relevant in the context of LPBF, where rapid solidification rates on the order of 10^5 – 10^6 K/s, coupled with steep

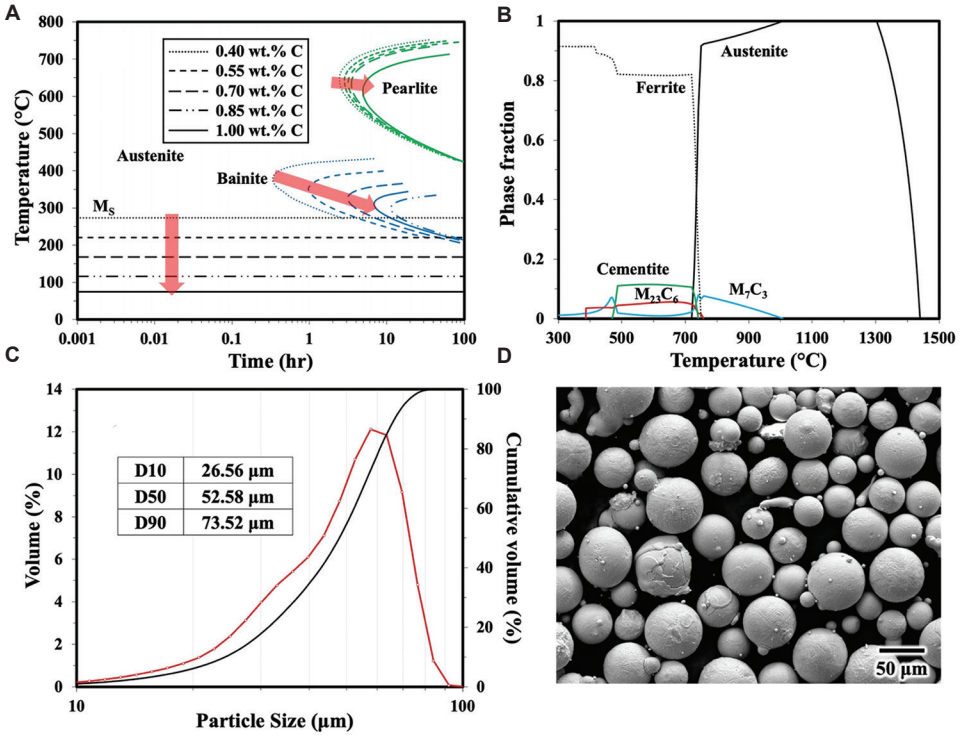

Figure 1. Materials selection and gas atomized alloy powders. (A) Time-temperature-transformation (TTT) diagram of the present alloy with varying carbon concentrations calculated using JMatPro™ (version 7). Red arrows indicate the decreasing martensite start (M_s) temperature as a function of increasing carbon concentration. (B) Phase fraction calculated using JMatPro™ (version 7) based on the nominal composition. (C and D) Particle size distribution (C) and secondary electron micrograph (D) of gas-atomized powders

thermal gradients, can impact phase transformations and the resulting microstructure. LPBF-fabricated parts commonly exhibit cellular dendritic microsegregation of alloying elements,[23,27,28] leading to spatial variations in local composition at the sub-micron scale, which can deviate from the nominal alloy chemistry.

These compositional inhomogeneities can significantly influence phase stability and transformation behavior, making it difficult to accurately predict or control the final microstructure based solely on nominal compositions. To address this, calculating the M_S temperature across a range of carbon concentrations offers valuable insight into phase stability during LPBF. As displayed in Figure 1A, the M_S temperature decreases substantially with increasing carbon content – dropping to approximately, 116°C at 0.85 wt.% C, and further to ~74°C at 1 wt.% C. Coupled with rapid solidification inherent to LPBF and a relatively low substrate temperature of 100°C, it becomes feasible to suppress martensitic transformation below room temperature at higher carbon levels. This would enable the retention of a predominantly austenitic matrix in the as-printed state. Accordingly, the primary focus of this study is to exploit the rapid cooling rates in LPBF and the elevated carbon content to produce a predominantly austenitic as-built alloy, which can then be subsequently heat treated to develop complex, hierarchical micro-constituents.

Pre-alloyed charges were inductively melted and gas-atomized using an-house double-induction gas atomizer. Metal charges were melted under ultra-high purity argon (99.99%), shrouded in an alumina crucible, and atomized using ultra-high purity argon pre-set to 3 MPa. Gas atomized powders were mechanically sieved using an industry-standard No. 200 (75 µm) sieve compatible with a Ro-Tap™ mechanical shaker. Particle size was verified using a laser diffraction particle size analyzer (Beckman Coulter LS™ 13 320; Beckman Coulter, United States to obtain a particle size distribution suitable for LPBF outlined in Figure 1C. The powder morphology is featured in Figure 1D, and the composition of the powders reported in Table 1 was measured using X-ray energy-dispersive spectroscopy (XEDS).

X-ray diffraction (XRD) patterns were acquired using a PANalytical Empyrean™ diffractometer (Malvern Panalytical, the Netherlands) equipped with a Cu K^{α} radiation source operating at 45 kV and 40 mA. The XRD patterns were obtained using a step size of 0.03°, dwell time of 60 s, and 2θ range between 30° and 85°. The direct

Table 1. Composition of powders and the as-printed sample determined by XEDS

ID	Composition (wt.%)										
	Fe	Si	Cr	Mo	Ni	Mn	V	C*	O*	N*	S*
Powders	Bal.	0.69±0.07	2.64±0.19	0.91±0.07	0.89±0.18	0.58±0.30	0.13±0.05	1.48	0.14	0.02	0.001
As-printed	Bal.	0.73±0.06	2.77±0.11	0.93±0.09	1.02±0.13	0.47±0.30	0.14±0.07	1.04	0.03	Neg.	0.001

Note: *Determined by LECO combustion analysis following ASTM E1019-18.
Abbreviation: XEDS: X-ray energy-dispersive spectroscopy.

comparison method was used to approximate the volume fraction of retained austenite (V^{γ}), from integrated intensities of γ(111) and α(110) diffraction peaks, $I^{\gamma}_{(111)}$ and $I^{\alpha}_{(110)}$, respectively, using the expression:[29,30]

$$V_{\gamma} = \frac{1.4 \times I_{\gamma(111)}}{I_{\alpha(110)} + 1.4 I_{\gamma(111)}} \quad (I)$$

In Equation I, carbide formation is assumed negligible and does not account for any signification volume fraction. Further microstructural examination of the optimized processing parameters was conducted using a scanning electron microscope (Zeiss Ultra 55 SEM; Carl Zeiss AG, Germany) operating at 20 kV equipped with an XEDS detector.

2.2. LPBF and sample preparation

Gas-atomized and sieved powders with a mean particle size of 53.7 μm were used to fabricate rectangular bars with dimensions of 8 × 8 × 100 mm in an SLM 125^{HL} system (Nikon-SLM Solutions, Germany equipped with a Yb-fiber laser capable of producing a spot size of 70 μm. Samples were fabricated directly on a stainless steel 316L substrate preheated to 100°C within an argon atmosphere at oxygen concentrations below 0.1%. Laser power, scan speed, hatch spacing, and slice thickness were held constant at 200 W, 800 mm/s, 120 μm, and 30 μm, respectively, from a cursory study of parameter optimization based on the highest relative density. The laser was scanned with 10 mm stripe widths at a constant interlayer rotation of 16°. The rectangular bars were removed from the substrate through wire electric discharge machining (EDM) without stress-relieving and cross-sectioned using a slow-speed diamond saw. Cross-sections were obtained parallel to the build direction and kept in the as-print condition to characterize for baseline reference. All cross-sectioned surfaces were mounted in epoxy resin and metallographically polished down to a 1 μm finish and chemically etched with 4% Nital.

Various post-processing treatments were performed to document the phase transformations of the as-printed samples as follows. As-printed samples were quenched in liquid nitrogen (LN_2) and held for 2.5 h to produce quenched martensite directly from the as-printed condition. Solutionizing treatment at 950, 1050, or 1075°C for 1 h, followed by water quenching, was also carried out to dissolve cellular dendrites apparent in the as-printed condition. Low-temperature tempering of as-printed samples was carried out with reference to Figure 1A at 125, 175, 200, 250, and 300°C for 3 h to probe the bainitic transformation as a function of temperature. Finally, a combination of cryogenic quenching, solutionizing, and tempering was carried out to obtain a mixed microstructure consisting of martensite, bainite, and austenite. The microhardness of the samples was measured using a LECO LV700 Vickers hardness indenter (LECO Corporation, United States) following ASTM E92-17 using a load of 10 kg and dwell time of 10 s. A total of five indents were performed for each sample to obtain sufficient statistical confidence.

3. Results

3.1. Martensitic transformation

Figure 2A presents the XRD pattern, and Figure 2B displays the austenitic microstructure characterized by fine cellular dendrites in the as-print specimen produced by LPBF. Qiao *et al.*[31] reported that the retained austenite, transforming to martensite in high-carbon steel after exposure to cryogenic conditions, exhibited a decrease from 12% after 2 h to approximately 10% after 48 h. Thus, a soak time of 2.5 h in LN_2 is reasonable for the majority of the austenite in the as-printed condition to transform. To explore the phase transformation of the austenitic microstructure observed in the as-printed condition, as-printed samples were quenched in liquid nitrogen at room temperature for up to 2.5 h. As displayed in Figure 2A, the intensity of the austenitic (γ) peak at 43.3° observed for the quenched sample is lower than that observed for the as-printed sample. The martensitic (M) peak observed just to the right of the γ(111) peak has become the dominant phase after quenching, which indicates that the austenite retained at room temperature has transformed into martensite, approximately 76 vol.%, after quenching in LN_2. The evidence for the transformation of the as-printed austenitic microstructure depicted in Figure 2B can be seen in the secondary electron micrograph in Figure 2C. Here, the

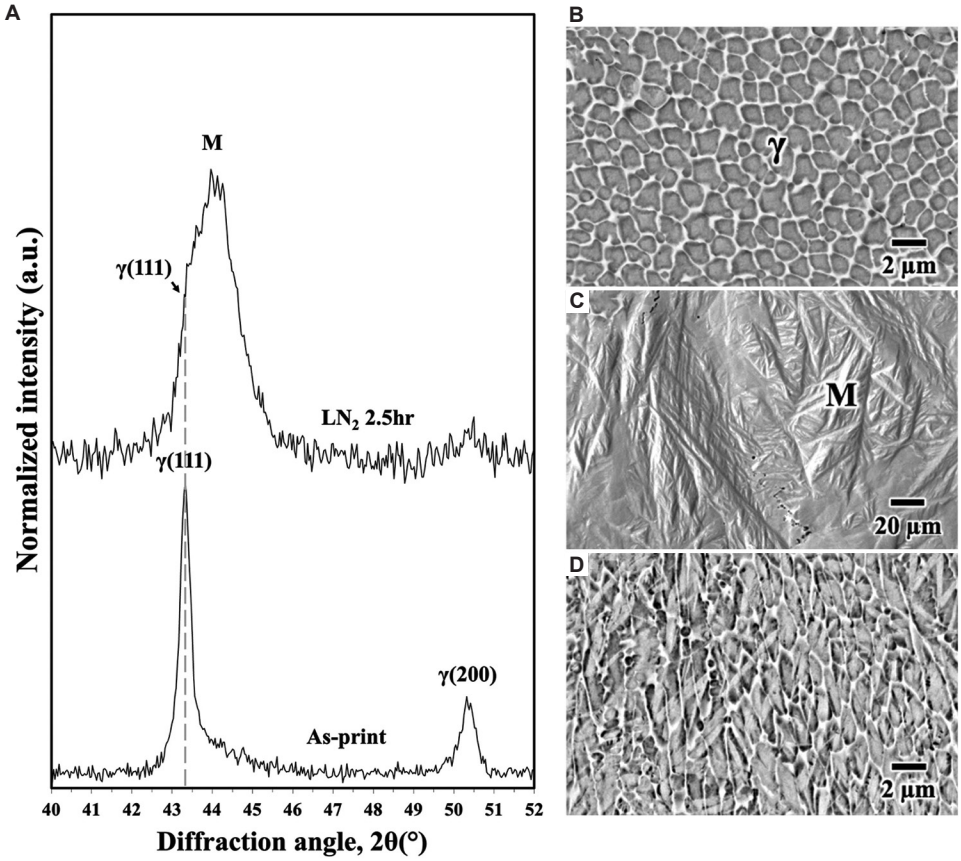

Figure 2. Macrostructural characteristics of the as-printed samples. (A) X-ray diffraction patterns of the as-printed sample and the sample quenched in LN_2 for 2.5 h. (B-D) Electron micrographs of the as-printed (B) and quenched samples (C and D)

surface undulations from the displacive movements of the martensitic transformation after cryogenic quench were visible. Since no reconstructive phase transformation has occurred, the backscatter electron (BSE) micrograph of the quenched sample in Figure 2D demonstrated that the cellular dendrites from the rapid solidification process still decorate the microstructure, which can be dissolved by solutionizing treatment.

3.2. Solutionizing treatment

Figure 3 compares the XRD patterns from the as-printed sample and those solutionized at 950, 1050, and 1075°C for 1 h. The as-printed sample consisted primarily of austenite with peaks observed at 43.3°, 50.4°, and 73.9°. When solutionized at 950°C for 1 h, the now convoluted γ(111) peak exhibited a slight shift to a higher 2θ, with a more dominant peak appearing roughly at the 2θ position for martensite, which accounted for approximately 90 vol.%. The rightward shift is most likely due to the outward diffusion of C and Cr from the supersaturated matrix to form carbides. When solutionized at 1050 and 1075°C, the austenitic peak was pronounced, and the convoluted martensitic or ferritic peak was noticeably less dominant compared to the 950°C solutionizing temperature. Particularly for the 1075°C anneal, the dominant austenitic peak is approximated to be 45 vol.%.

Findings from XRD were confirmed by electron micrographs presented in Figure 4. The as-printed microstructure in Figure 4A is primarily austenitic, decorated by fine cellular dendrites with some martensite growing across multiple cells. After solutionizing at 950°C for 1 h, the cellular microstructure was replaced by carbides nucleated within and along the grain boundaries. These carbides are predicted to be M_7C_3 according to thermodynamic calculations presented in Figure 1B.

No cells were observed within the matrix, which indicates that the solutionizing treatment at this temperature is sufficient for the dissolution of cells. Although the sample was immediately quenched in water, partial formation of martensite or Widmanstätten ferrite within the austenite grains was observed. The microstructure of the sample solutionized at 1050°C for 1 h also highlights the dissolution of cells; however, the number of carbides observed is much

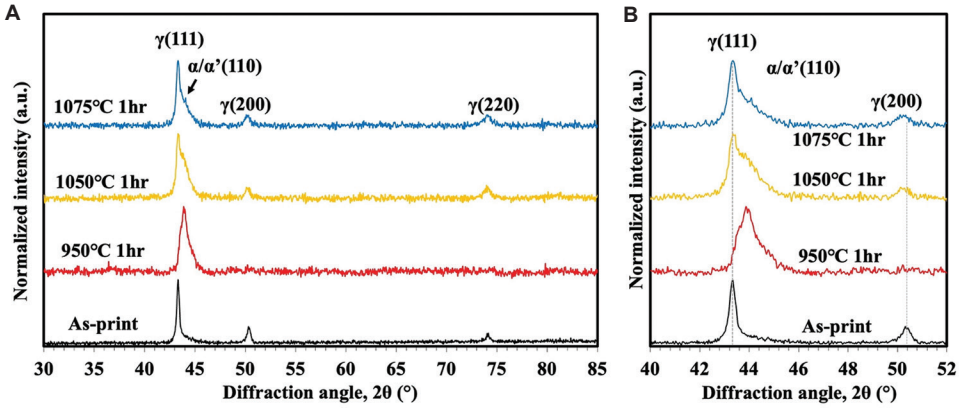

Figure 3. Phase constituents after solution heat treatment. (A) Overall XRD patterns collected from the XZ-cross-sections solutionized at various temperatures. (B) Detailed 2θ pattern from 40° to 52°
Abbreviations: XRD; X-ray diffraction

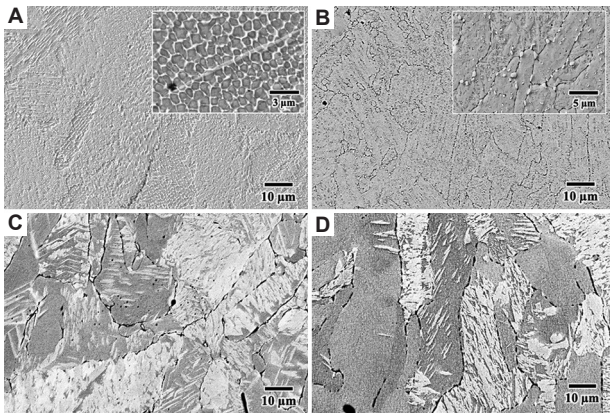

Figure 4. Backscatter electron micrographs of samples (A) as printed, (B) solutionized at 950°C for 1 h, (C) solutionized at 1050°C for 1 h, and (D) solutionized at 1075°C for 1 h

lower compared to that seen in Figure 4B. Interestingly, the white phase observed within the grains closely resembles that of plate-like Widmanstätten ferrite nucleated from the austenite grain boundaries and growing directionally within the austenite grains. Solutionizing at 1075°C for 1 h resulted in the total dissolution of cells, and the matrix was practically carbide-free; however, some Widmanstätten ferrite was still observed.

3.3. Bainitic transformation

Researchers have produced lower-bainite steels with high hardness and toughness by heat treatment at moderately low temperatures.[32,33] The steel examined in this study has austenite stability at room temperature, and it was reported that some martensite existed within the microstructure when printed on a substrate preheated at 100°C. While 100°C could be high enough for the formation of bainite to occur, the sluggish kinetics would require an extended annealing duration for the first bainitic ferrites to form at this temperature. To document the bainitic transformation, it is necessary to increase the annealing temperature to accelerate the transformation rate in the as-printed sample. Figure 5 presents the XRD patterns for the transformation of bainite at 125, 175, 200, 250, and 300°C for 3 h. As the transformation temperature increased, the fraction of bainite increased from approximately 35 vol.% at 125°C to 45 vol.% at 300°C. Figure 6B displays that some lower bainite could form at temperatures as low as 125°C. At 175 °C, the bainite sheaves appeared long and slender. Increasing the annealing temperature to 200 °C and 250 °C resulted in only a slight coarsening of the sheaves when transformed at 300°C for 3 h (Figure 6F), the sheaves became much coarser with additional aggregates of shorter and slimmer sheaves growing around them.

Young and Bhadeshia.[34] demonstrated that in a 0.4 wt.% C high-strength steel containing a mix of martensite and bainite, the strength contribution of bainite increased to a maximum when the fraction of bainite was 20%. Above 20%, the strength of the alloy decreased continuously and reached a minimum when fully bainitic steel was obtained. In other words, if the present alloy is heat treated at too high of a temperature, the higher fraction of transformed bainite could significantly soften the alloy. As evident from the XRD patterns and the microstructures featured in Figures 5 and 6, it is necessary to adopt a low-temperature rather than a high-temperature treatment for bainitic transformation. The sluggish reconstructive phase transformation at low temperatures would require an extended period of time for any substantial increase in the fraction of bainite to severely weaken the overall matrix. As such, the lower bainite transformation at 175°C for 3 and 24 h is presented in Figure 7A and B, respectively. The initial nucleation of bainite was clearly visible in the etched micrographs. After 24 h exposure at 175°C, no substantial

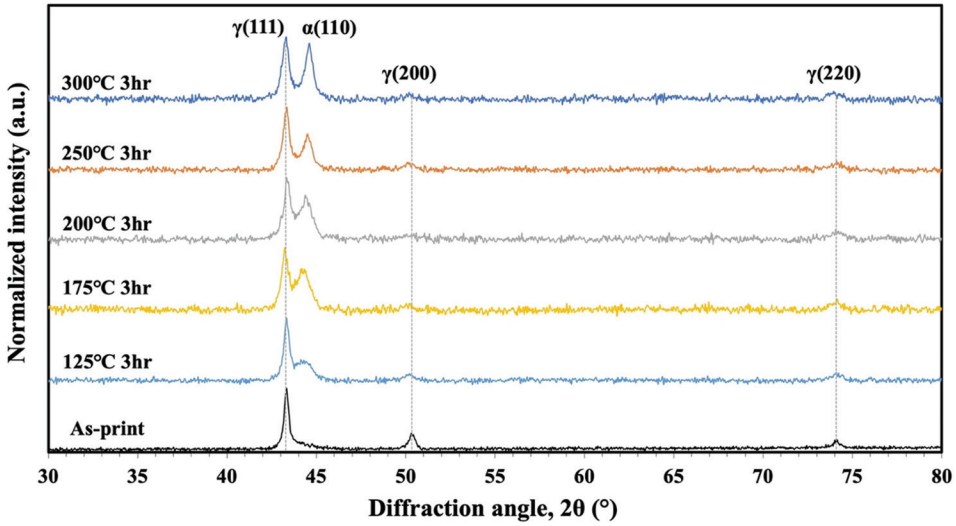

Figure 5. X-ray diffraction patterns of as-printed samples annealed at various bainitic transformation temperatures for 3 h

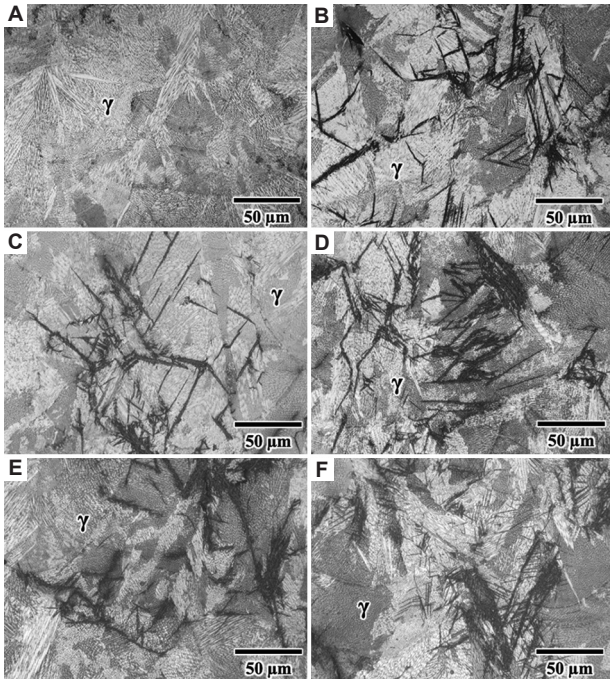

Figure 6. Optical micrographs of the as-printed sample (A) and annealed samples at (B) 125°C for 3 h, 175°C for 3 h (C), 200°C for 3 h (D), 250°C for 3 h (E), and 300°C for 3 h (F). The bainite etches are denoted as dark contrasts

increase in the amount of bainite was observed even after the prolonged isothermal treatment.

3.4. Multi-phase high-carbon-bearing steel

It has been demonstrated thus far that the as-printed microstructure can be solutionized, quenched, and annealed to obtain "cell-free," quenched martensite

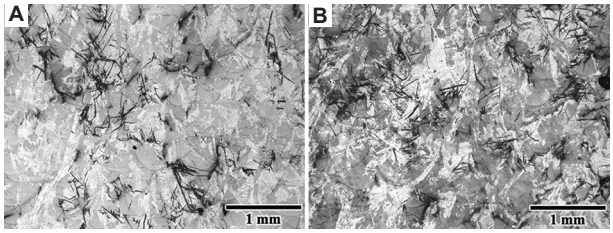

Figure 7. Optical micrograph of samples annealed at 175°C for (A) 3 h and (B) 24 h. Bainite etches are indicated in dark shades. Scale bars: 1 mm

or bainite, all of which still possess a large fraction of austenite available for further transformation in a multi-step process. First, a matrix consisting of quenched martensite and bainite could be obtained (Figure 8A). The combination of quenching in LN_2 for 2.5 h, followed by heat treatment at 175°C for 1 h, yielded islands of austenite, along with martensite and bainite adorned with cellular dendrites. The large, interconnected network of cells made it challenging to distinguish between martensite and bainite. Figure 8B displays the microstructure of the sample solutionized at 1075°C for 1 h, quenched in LN_2 for 2.5 h, and then heat treated at 175°C for 1 h. The resulting microstructure is, however, a mix of austenite, martensite, and bainite, without the cellular network. It is much easier to distinguish between the different phases in this microstructure. As presented in Figure 8B, the bainite sheaves, which generally etch dark, were observed to have nucleated at the boundary of the plate martensite and grew across the retained austenite island. The nucleation of bainite along the γ/α' interface is preferred,[35] and this mechanism is likely similar to that observed in the quenched and tempered condition presented in Figure 8A.

3.5. Microhardness

Compared to the hardness of 344 ± 21 HV in the as-printed sample, a quench in LN_2 for 2.5 h at room temperature for the as-printed samples yielded a hardness increase as high as 737 ± 31 HV – the ultrahigh hardness of quenched martensite. Similarly, the solutionizing treatment at 950°C for 1 h effectively doubled the as-printed hardness to 712 ± 15 HV due to precipitation of carbides instead of martensite. However, at higher solutionizing temperatures of 1050 and 1075°C, the hardness decreased to 303 ± 10 and 259 ± 1.4 HV, respectively. These lower hardness values indicate the effective dissolution of cells and the absence of carbides to form the predominantly austenitic microstructure. Although an excellent hardness was obtained for the directly quenched sample, it is likely to be brittle.

With the addition of bainite, the brittle matrix may soften but partially compensated by increased toughness. Figure 9 plots the microhardness of the as-printed sample along with samples that were LN_2-quenched and had various multi-step heat treatments. LPBF samples quenched in LN_2 and annealed at 175°C for 1 h retained a hardness of 690 ± 31 HV. Even after 125 h at 175°C, the hardness remained at 682 ± 16 HV. This suggests

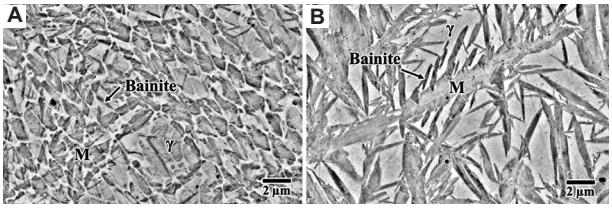

Figure 8. Backscatter electron micrographs of samples (A) quenched in LN_2 for 2.5 h and annealed at 175°C for 1 h, and (B) solutionized at 1075°C for 1 h, quenched in LN_2 for 2.5 h, and annealed at 175°C for 1 h. Scale bars: 2 μm.

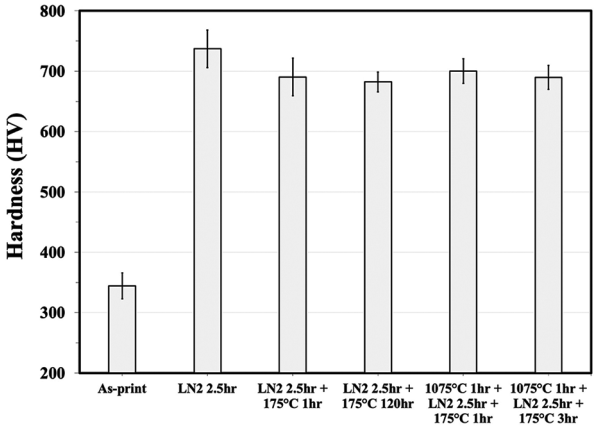

Figure 9. Vickers hardness of as-printed and post-processed conditions ($n = 5$)

the sluggish kinetics of bainite development at 175°C (Figure 7). Compared to the as-printed alloy, the slight decrease in hardness after the 175°C-exposure could be a combination of C partition from supersaturated martensite and the nucleation of bainite.

With the additional solutionizing treatment at 1075°C before LN_2-quenching and annealing at 175°C for 1 h, the microhardness measured was as high as 700 ± 20 HV. After 3 h at 175°C, the hardness remained relatively high at approximately 690 ± 20 HV, only reducing by ~6% after 1 h and ~7% after 120 h at 175°C, when the alloy was directly quenched and tempered after LPBF. For the alloy solutionized at 1075°C, a reduction in hardness of only ~5% was observed after quenching and tempering.

4. Discussion

The microstructures observed in samples solutionized at 1050 and 1075°C suggest the formation of Widmanstätten ferrite rather than martensitic or bainitic structures, supported by several key observations. First, elevated solutionizing temperatures promote coarse austenite grain structures,[36,37] and when combined with relatively rapid cooling, are known to favor the development of Widmanstätten ferrite.[38] This transformation can occur with very low driving forces – significantly lower than those required for diffusionless transformations such as martensite.[39] Second, solution treatment above the carbide precipitation temperature leads to the saturation of carbon and alloying elements in austenite, which further suppresses the M_S temperature, likely lowering it below ambient conditions. This suppression is corroborated by microhardness measurements in both the as-printed and solutionized conditions. The as-printed sample exhibited a hardness of 344 ± 21 HV, while samples solutionized at 1050 and 1075°C displayed reduced hardness values of 303 ± 10 and 259 ± 1.4 HV, respectively. Although austenite is generally softer than ferrite, the higher hardness of the as-printed austenitic matrix can be attributed to its finer grain size and higher dislocation density – both resulting from the rapid solidification inherent to LPBF. In contrast, solution treatment leads to recrystallization and/or grain growth, as well as dislocation annihilation, which collectively reduce hardness, as displayed in Figure 5C and D.

To further confirm the absence of martensitic transformation after solutionizing, a sample was solutionized at 1075°C, water-quenched, and then submerged in liquid nitrogen for 2.5 h. This sample exhibited a microhardness of 683 ± 20 HV, similar to that of the as-printed sample directly quenched in LN_2

without prior solutionizing. These results suggest that martensite did not form during water quenching after the solutionizing step but only developed during the subsequent cryogenic treatment in LN_2. In addition, direct water quenching at 1050 or 1075°C is not expected to yield lower bainite due to the inherently slow transformation kinetics. No evidence of lower bainite was observed in the water-quenched microstructure.

Microsegregation in the as-printed microstructure leads to compositional variations between cellular and intercellular regions, which can significantly influence phase transformation behavior. As featured in Figure 1A, TTT curves for a homogeneous matrix with varying carbon content indicate that bainitic transformation is not expected to occur at temperatures as low as 125°C after 3 h. However, the segregation of carbon in the form of carbides[40] and substitutional alloying elements, such as Mo, Cr, Mn, and Si, to intercellular regions,[28,41,42] as observed in Figure 3B, may dramatically alter the bainite start temperature and incubation period.[43] Thus, the microstructural heterogeneity induced by the rapid solidification inherent to LPBF plays a critical role in altering transformation pathways, potentially enabling bainite formation that would not be predicted based on nominal compositions alone.

5. Conclusion

Additively manufactured high-carbon-bearing steel with solidified austenite primed for phase transformations was investigated for microstructural evolution. Excellent hardness, as high as 737 ± 31 HV, was achieved with a liquid-nitrogen quench at room temperature for the as-printed condition. The high-solutionizing temperature can be tailored to produce carbide or carbide-free matrices, and the amount of desired carbides could be controlled by the temperature of the solutionizing treatment. A multi-phase microstructure consisting of austenite, martensite, and bainite with excellent hardness was achieved by altering the microstructure with heat treatments. Results demonstrated that LPBF of high-carbon-bearing steels possess intriguingly controllable microstructures and a wide range of mechanical properties that can be tailored to the desired application.

Acknowledgments

None.

Funding

This research was sponsored by the DEVCOM Army Research Laboratory under a cooperative agreement contract, W911NF1720172.

Conflicts of interest

Yongho Sohn serves as the Editorial Board Member of the journal but was not in any way involved in the editorial and peer-review process conducted for this paper, directly or indirectly. The other authors declare they have no competing interests. In addition, the views, opinions, and conclusions made in this document are those of the authors and should not be interpreted as representing the official policies, either expressed or implied, of the DEVCOM Army Research Laboratory or the U.S. Government. The U.S. Government is authorized to reproduce and distribute reprints for Government purposes notwithstanding any copyright notation herein.

Authors' contributions

Conceptualization: Thinh Huynh, Yongho Sohn
Formal analysis: Thinh Huynh
Investigation: Thinh Huynh, Kevin Graydon, Nicolas Ayers
Methodology: Thinh Huynh, Yongho Sohn
Validation: Kevin Graydon, Nicolas Ayers, Yongho Sohn
Writing – original draft: Thinh Huynh
Writing – review and editing: Yongho Sohn

Ethics approval and consent to participate

Not applicable.

Consent for publication

Not applicable.

Availability of data

All data associated with this publication are available upon request from the corresponding author.

References

1. Mehta A, Zhou L, Huynh T, *et al*. Additive manufacturing and mechanical properties of the dense and crack free Zr-modified aluminum alloy 6061 fabricated by the laser-powder bed fusion. *Addit Manuf*. 2021;41:101966.

   doi: 10.1016/j.addma.2021.101966

2. Zhou L, Hyer H, Park S, *et al*. Microstructure and mechanical properties of Zr-modified aluminum alloy 5083 manufactured by laser powder bed fusion. *Addit Manuf*. 2019;28:485-496.

   doi: 10.1016/j.addma.2019.05.027

3. Zheng B, Zhou Y, Smugeresky J, Schoenung J, Lavernia E. Thermal behavior and microstructural evolution during laser deposition with laser-engineered net shaping: Part I. Numerical calculations. *Metall Mater Trans A*. 2008;39:2228-2236.

   doi: 10.1007/s11661-008-9557-7

4. Krakhmalev P, Yadroitsava I, Fredriksson G, Yadroitsev I. *In situ* heat treatment in selective laser melted martensitic AISI 420 stainless steels. *Mater Des*. 2015;87:380-385.

doi: 10.1016/j.matdes.2015.08.045

5. Jelis E, Clemente M, Kerwien S, Ravindra NM, Hespos MR. Metallurgical and mechanical evaluation of 4340 steel produced by direct metal laser sintering. *JOM J Miner Metals Mater Soc*. 2015;67:582-589.

doi: 10.1007/s11837-014-1273-8

6. Shakerin S, Hadadzadeh A, Amirkhiz BS, Shamsdini S, Li J, Mohammadi M. Additive manufacturing of maraging steel-H13 bimetals using laser powder bed fusion technique. *Addit Manuf*. 2019;29:100797.

doi: 10.1016/j.addma.2019.100797

7. Fonseca EB, Gabriel AH, Araújo LC, Santos PL, Campo KN, Lopes ES. Assessment of laser power and scan speed influence on microstructural features and consolidation of AISI H13 tool steel processed by additive manufacturing. *Addit Manuf*. 2020;34:101250.

doi: 10.1016/j.addma.2020.101250

8. Lee J, Choe J, Park J, Yu J-H, Kim S, Sung H. Microstructural effects on the tensile and fracture behavior of selective laser melted H13 tool steel under varying conditions. *Mater Charact*. 2019;155:109817.

doi: 10.1016/j.matchar.2019.109817

9. Yan J, Zheng D, Li H, *et al*. Selective laser melting of H13: Microstructure and residual stress. *J Mater Sci*. 2017;52:12476-12485.

doi: 10.1007/s10853-017-1380-3

10. Zhang M, Chen C, Qin L, *et al*. Laser additive manufacturing of M2 high-speed steel. *Mater Sci Technol*. 2018;34(1):69-78.

doi: 10.1080/02670836.2017.1355584

11. Zumofen L, Beck C, Kirchheim A, Dennig HJ. Quality Related Effects of the Preheating Temperature on Laser Melted High Carbon Content Steels. In: *Industrializing Additive Manufacturing - Proceedings of Additive Manufacturing in Products and Applications - AMPA2017*. Cham: Springer; 2018. p. 210-219.

doi: 10.1007/978-3-319-66866-6_21

12. Huber F, Bischof C, Hentschel O, *et al*. Laser beam melting and heat-treatment of 1.2343 (AISI H11) tool steel-microstructure and mechanical properties. *Mater Sci Eng A*. 2019;742:109-115.

doi: 10.1016/j.msea.2018.11.001

13. Saewe J, Gayer C, Vogelpoth A, Schleifenbaum JH. Feasability investigation for laser powder bed fusion of high-speed steel AISI M50 with base preheating system. *Berg Huettenmaenn Monatsh*. 2019;164:101-107.

doi: 10.1007/s00501-019-0828-y

14. Boes J, Röttger A, Mutke C, Escher C, Theisen W. Microstructure and mechanical properties of X65MoCrWV3-2 cold-work tool steel produced by selective laser melting. *Addit Manuf*. 2018;23:170-180.

doi: 10.1016/j.addma.2018.08.005

15. Taha M, Yousef A, Gany K, Sabour H. On selective laser melting of ultra high carbon steel: Effect of scan speed and post heat treatment. *Materialwissenschaft Werkstofftechnik*. 2012;43(11):913-923.

doi: 10.1002/mawe.201200030

16. Casati R, Coduri M, Lecis N, Andrianopoli C, Vedani M. Microstructure and mechanical behavior of hot-work tool steels processed by selective laser melting. *Mater Charact*. 2018;137:50-57.

doi: 10.1016/j.matchar.2018.01.015

17. Yuan M, Cao Y, Karamchedu S, *et al*. Characteristics of a modified H13 hot-work tool steel fabricated by means of laser beam powder bed fusion. *Mater Sci Eng A*. 2022;831:142322.

doi: 10.1016/j.msea.2021.142322

18. Holzweissig MJ, Taube A, Brenne F, Schaper M, Niendorf T. Microstructural characterization and mechanical performance of hot work tool steel processed by selective laser melting. *Metall Mater Trans B*. 2015;46:545-549.

doi: 10.1007/s11663-014-0267-9

19. Kempen K, Vrancken B, Buls S, Thijs L, Van Humbeeck J, Kruth JP. Selective laser melting of crack-free high density M2 high speed steel parts by baseplate preheating. *J Manuf Sci Eng*. 2014;136(6):061026.

doi: 10.1115/1.4028513

20. Tan C, Li R, Su J, *et al*. Review on field assisted metal additive manufacturing. *Int J Mach Tools Manuf*. 2023;189:104032.

doi: 10.1016/j.ijmachtools.2023.104032

21. Dilip J, Ram GJ, Starr TL, Stucker B. Selective laser melting of HY100 steel: Process parameters, microstructure and mechanical properties. *Addit Manuf*. 2017;13:49-60.

doi: 10.1016/j.addma.2016.11.003

22. Kudzal AD, McWilliams BA, Taggart-Scarff J, Knezevic M. Fabrication of a low alloy ultra-high strength (>1500 MPa yield) steel using powder bed fusion additive manufacturing. *Mater Sci Eng A*. 2020;770:138512.

doi: 10.1016/j.msea.2019.138512

23. Seede R, Shoukr D, Zhang B, *et al*. An ultra-high strength martensitic steel fabricated using selective laser melting additive manufacturing: Densification, microstructure, and mechanical properties. *Acta Mater*. 2020;186:199-214.

doi: 10.1016/j.actamat.2019.12.037

24. Zhang S, Wang Q, Yang R, Dong C. Composition equivalents

of stainless steels understood via gamma stabilizing efficiency. *Sci Rep*. 2021;11(1):5423.

doi: 10.1038/s41598-021-84917-z

25. Seede R, Zhang B, Whitt A, *et al*. Effect of heat treatments on the microstructure and mechanical properties of an ultra-high strength martensitic steel fabricated via laser powder bed fusion additive manufacturing. *Addit Manuf*. 2021;47:102255.

doi: 10.1016/j.addma.2021.102255

26. Agrawal P, Shukla S, Thapliyal S, *et al*. Microstructure-property correlation in a laser powder bed fusion processed high-strength AF-9628 steel. *Adv Eng Mater*. 2021;23(1):2000845.

doi: 10.1002/adem.202000845

27. Aguilar F, Huynh T, Kljestan N, Knezevic M, Sohn Y. Microstructure and mechanical characterization of AISI 4340 steel additively manufactured by laser powder bed fusion. *Metals*. 2025;15(4):412.

doi: 10.3390/met15040412

28. Yao J, Tan Q, Venezuela J, Atrens A, Zhang MX. Additive manufacturing of high-strength low-alloy AISI 4340 steel with an optimal strength-ductility-toughness trade-off. *Addit Manuf*. 2024;94:104496.

doi: 10.1016/j.addma.2024.104496

29. Song Y, Li X, Rong L, Li Y. The influence of tempering temperature on the reversed austenite formation and tensile properties in Fe–13%Cr–4%Ni–Mo low carbon martensite stainless steels. *Mater Sci Eng A*. 2011;528(12):4075-4079.

doi: 10.1016/j.msea.2011.01.078

30. Tanaka M, CHOI CS. The effects of carbon contents and Ms temperatures on the hardness of martensitic Fe-Ni-C Alloys. *Trans Iron Steel Inst Japan*. 1972;12(1):16-25.

doi: 10.2355/isijinternational1966.12.16

31. Qiao X, Han L, Zhang W, Gu J. Thermal stability of retained austenite in high-carbon steels during cryogenic and tempering treatments. *ISIJ Int*. 2016;56(1):140-147.

doi: 10.2355/isijinternational.ISIJINT-2015-248

32. Garcia-Mateo C, FG C, HKDH B. Development of hard bainite. *ISIJ Int*. 2003;43(8):1238-1243.

doi: 10.2355/isijinternational.43.1238

33. Caballero FG, Bhadeshia HKD. Very strong bainite. *Curr Opin Solid State Mater Sci*. 2004;8(3-4):251-257.

doi: 10.1016/j.cossms.2004.09.005

34. Young CH, Bhadeshia HKD. Strength of mixtures of bainite and martensite. *Mater Sci Technol*. 1994;10(3):209-214.

doi: 10.1179/mst.1994.10.3.209

35. Kawata H, Hayashi K, Sugiura N, Yoshinaga N, Takahashi M. Effect of martensite in initial structure on bainite transformation. *Mater Sci Forum*. 2010;638-642:3307-3312.

doi: 10.4028/www.scientific.net/MSF.638-642.3307

36. Bodnar RL, Hansen SS. Effects of austenite grain size and cooling rate on Widmanstätten ferrite formation in low-alloy steels. *Metall Mater Trans A*. 1994;25:665-675.

doi: 10.1007/BF02665443

37. Cochrane R, Mintz B, Ward J. Influence of prior microstructure on normalising response of C–Mn–Al–Nb steels. *Mater Sci Technol*. 1989;5(1):20-28.

doi: 10.1179/mst.1989.5.1.20

38. Krauss G. *Steels: Processing, Structure, and Performance*. United States: ASM International; 2015.

39. Bhadeshia HKDH, Honeycombe RWK. *Steels: Microstructure and Properties*. United Kingdom: Butterworth-Heinemann; 2017.

40. Chou CY, Pettersson NH, Durga A, *et al*. Influence of solidification structure on austenite to martensite transformation in additively manufactured hot-work tool steels. *Acta Mater*. 2021;215:117044.

doi: 10.1016/j.actamat.2021.117044

41. Kim KS, Kim YK, Yang S, Koo B, Lee KA. Microstructure and mechanical properties of carbon-bearing ultrahigh-strength high Co-Ni Steel (AerMet 340) fabricated via laser powder bed fusion. *Materialia*. 2021;20:101244.

doi: 10.1016/j.mtla.2021.101244

42. Krell J, Röttger A, Geenen K, Theisen W. General investigations on processing tool steel X40CrMoV5-1 with selective laser melting. *J Mater Process Technol*. 2018;255:679-688.

doi: 10.1016/j.jmatprotec.2018.01.012

43. Wang J, Van Der Wolk P, Van Der Zwaag S. On the influence of alloying elements on the bainite reaction in low alloy steels during continuous cooling. *J Mater Sci*. 2000;35:4393-4404.

doi: 10.1023/A:1004865209116